

Two Scale FE Simulation of Coated Forming Tools under Thermo-Mechanical Loading

K.-H. Sauerland, R. Mahnken

Modern trends and challenges in manufacturing processes have led to an increasing complexity of hybrid forming processes in the last couple of years. Besides the improvement of the thermo-mechanical process chain the application of coated forming tools plays a crucial role in actual developments. Considering machining processes in general the investigation of tools experienced a secondary role in the past. For example, in numerical simulations of manufacturing processes tools are often modelled as rigid bodies. To remedy, this paper introduces a two scale finite element model for the coating system of a coated hybrid forming tool. Within this concept individual coating layers are considered on the mesoscale and macroscopic results for the coating elements are obtained using volume averaging procedures. Two numerical examples using an implicit and an explicit integration scheme show the capability of the model to be applied for a coated forming tool subjected to thermo-mechanical loading conditions.

1 Introduction

In the recent past the complexity of forming processes has increased by far due to the ongoing demand of high-quality components produced under manufacturing conditions strongly related to the ambitious goals of energy and cost efficiency. For example, two potential possibilities to enhance traditional hybrid forming processes are improvements in the thermo-mechanical process chain (Steinhoff et al., 2005; Weidig et al., 2008) or application of forming tools showing a higher complexity in their thermo-mechanical behavior. Considering the latter case and generalizing it to other manufacturing processes like cutting, turning or milling, coated tools play an important role in actual machining processes (Liu et al., 2009; Uzun and Aslantas, 2011). Besides the increasing complexity of products and processes, additionally simulation methods have been improved in the last decades and have become standard tools for investigation and analysis due to the upgraded availability of computational power. Consequently, nowadays finite element simulations of workpieces, tools and machining processes have received great attention and are actually applied for prediction of, e.g., microstructure evolutions, temperatures, cutting forces, stresses or tool lifetimes. To motivate this paper, in the following the issues of phenomenological simulation of bulk metal forming, multiscale methods and numerical simulation of coatings are discussed.

Phenomenological simulation of bulk metal forming processes has gained more and more attention in recent years, since finite element software and computational hardware have been improved for several dimensions in the last decades. Up to now, Lagrangian and Eulerian formulations, fixed meshed, adaptive refined meshed and element free models, implicit and explicit integration schemes as well as linear and nonlinear solution procedures have been developed at universities or in industry in order to focus on many different phenomena involved in bulk metal forming. Intending to give a short survey on the large field of phenomenological simulations of these processes, subsequently some publications using different approaches are addressed briefly. E.g. Li et al. (2001) apply a Lagrangian formulation with remeshing and an implicit and explicit integration scheme for solution of the nonlinear equations occurring during simulation of open die forging and forward extrusion processes. Contrary, Lu et al. (2008) use an element free Galerkin method for the numerical simulation of cubic billet upsetting. In addition, Xiong et al. (2005) perform numerical simulations of compression of cylindrical preforms using an element free model as well as a model with a fixed finite element mesh. Moreover, Saanouni (2008) applies a fixed finite element mesh for the two-dimensional simulation of sidepressing of cylindrical bars. To summarize the large field of issues and applications, see for example Hartley and Pillinger (2006), phenomenological simulation of bulk metal forming processes has become a kind of standard tool for process investigation, but the particular approaches are quite different. Within the large amount of scientific publications particular topics as process modelling, tool design, interface phenomena or material phenomena besides others are of main interest in current research.

The increasing computational power in the last decades has also led to the development of multiscale methods used for simulation of a wide range of components and processes. Within this field, a lot of scientific work has been done by Geers et al. (Kouznetsova et al., 2001; Özdemir et al., 2008a,b). Kouznetsova et al. (2001) introduce a micro-macro strategy suitable for modelling of the mechanical response of heterogeneous materials at large deformations and non-linear history-dependent material behavior. Within this strategy there is no need to specify the homogenized constitutive behavior, since this behavior is determined through the detailed modelling of the microstructure. Özdemir et al. (2008a) propose a multiscale analysis method for heat transfer in heterogeneous solids. The introduced method extends a two scale computational homogenization approach, which is applied for the stress analysis of multi-phase solids under purely mechanical loading. Further, Özdemir et al. (2008b) apply a two scale thermo-mechanical analysis framework for heterogeneous solids based on computational homogenization techniques. The proposed framework does not require explicitly determined homogenized material properties, since no constitutive equations are required on the macrolevel. Additionally, multiscale methods have been applied extensively by Miehe et al. (Miehe and Koch, 2002; Miehe and Dettmar, 2004). Miehe and Koch (2002) investigate algorithms for the computation of homogenized stresses and overall tangent moduli of microstructures undergoing small strains. In this context, three classical types of boundary conditions are investigated, in particular linear displacements, constant tractions and periodic displacements combined with antiperiodic tractions. Further, Miehe and Dettmar (2004) introduce an approach for modelling of the overall macroscopic response of periodic granular materials based on a numerically evaluated micro-to-macro transition. In this approach a homogenized macro-continuum with locally attached microstructure is considered, representing an aggregate of discrete solid granules which possibly come into contact. Furthermore, many other works have been published in the past few years concerning multiscale modelling (Allen, 2001; Feyel and Chaboche, 2000; Bobzin et al., 2006). Allen (2001) applies homogenization principles to continuum damage mechanics. Results show a damage evolution law on the macroscale being no longer necessary, since the damage parameters resulting from the homogenization process are direct results of the micro-mechanical solution on the smaller scale. Feyel and Chaboche (2000) use a new multiscale behavior model based on a multilevel finite element (FE²) approach to take into account heterogeneities in the behavior between fibre and matrix of long fibre SiC/Ti composite materials. Results show that macroscopic constitutive equations are no longer necessary, if the FE² method is applied in combination with parallel computation, thus leading to a finite element simulation of the microstructure and on the macroscopic scale in an appropriate time. Bobzin et al. (2006) investigate advanced homogenization strategies in material modelling of thermally sprayed thermal barrier coatings. Results show homogenization for periodic structures combined with a multiperiodical approach reducing significantly the calculation time compared to the homogenization based on the physical equivalence.

In recent years many scientific works have been published concerning finite element simulation of coatings. Here, one part is addressed to the coating formation, as the coating process affects the coating microstructure influencing the thermo-mechanical properties of the final coating system. E.g. Lugscheider et al. (2006) investigate numerically the coating formation of atmospheric plasma sprayed partially yttria stabilized zirconia. To this end they perform a microscopic particle impact simulation and a macroscopic coating formation simulation. In addition, Feng et al. (2000) investigate the impact of a metal droplet onto a solid surface with different surface roughnesses using the finite element method. They apply a model based on the Lagrangian method with an automatic adaptive remeshing technique allowing for large deformations. Contrary, Wenzelburger et al. (2004) investigate the residual stress formation during thermal spraying. For this purpose they perform a heat transfer analysis followed by a thermal stress analysis of an aluminum tube with internal coating. Besides the investigation of the coating formation another part is addressed to the simulation of already coated parts and components. A detailed overview over the numerical treatment of coatings and surface modification technologies is given by Mackerle (2005). E.g. Xie et al. (2006) investigate the stress and cracking behavior of plasma sprayed thermal barrier coatings. To this end they introduce a viscoplastic material model with a non-associative flow rule for constitutive modelling of the ceramic thermal barrier layer. Liu et al. (2009) investigate the effects of coated tools on high speed orthogonal machining. In the applied finite element model a perfect plastic workpiece and a rigid tool are considered. Uzun and Aslantas (2011) perform numerical simulations of an orthogonal machining process using multilayer and single-layer coated tools. Again, the cutting tool is modelled as rigid body.

In this work we introduce a two scale FE model for coated forming tools under thermo-mechanical loading. Our intention is to combine the issues of phenomenological simulation of bulk metal forming, multiscale modelling and numerical simulation of coatings into one common research project. Moreover, we want to direct the main focus on the coated forming tool, since machining tools experienced a secondary role in the past. To this end we apply an elastic and an elasto-viscoplastic material model for the forming tool substrate, which is a large extension compared to other works using a rigid tool substrate. Additionally, a two scale model is applied for the coating system considering several individual layers with different thermo-mechanical behavior models on the mesolevel.

In general for two scale formulations often FE^2 is applied, see e.g. Feyel and Chaboche (2000); Özdemir et al. (2008a,b). One main disadvantage of FE^2 models are large computing times leading to high computational costs. To remedy, in our work we use a two scale model with one finite element over the coating thickness aiming for consideration of different material models for different coating layers. In the following the thermo-mechanical coupled two scale framework is outlined with particular emphasis on scale transitions and constitutive equations on the mesoscale. After that, remarks on numerical implementation are briefly outlined and finally two numerical examples are illustrated using an implicit and an explicit solution strategy.

2 Thermo-Mechanical Coupled Two Scale Framework

A two scale model is applied to the coating system of the coated hybrid forming tool, which consists of a macroscale and a mesoscale. A schematic representation of the two scale character is illustrated in Figure 1 with basic conceptions adopted by Özdemir et al. (2008a,b). The idea consists of a discretization of the complete coating system within one finite element over the thickness on the macroscale. For each integration point of the macro finite elements representing the coating a representative volume element (RVE) of the mesoscale is attached (see Figure 3). On the mesoscale within this RVE the particular coating layers are considered with possible different constitutive models and different material parameters. Of course, appropriate boundary conditions have to be transferred from the macrolevel onto the RVE of the mesolevel and, regarding the opposite case, suitable homogenization procedures have to be applied for determination of macroscopic results from the constitutive responses on the mesoscale. For description of the thermo-mechanical coupled two scale model in the following the macroscopic and mesoscopic boundary value problems (BVPs) and thermodynamic consistent scale transitions are introduced.

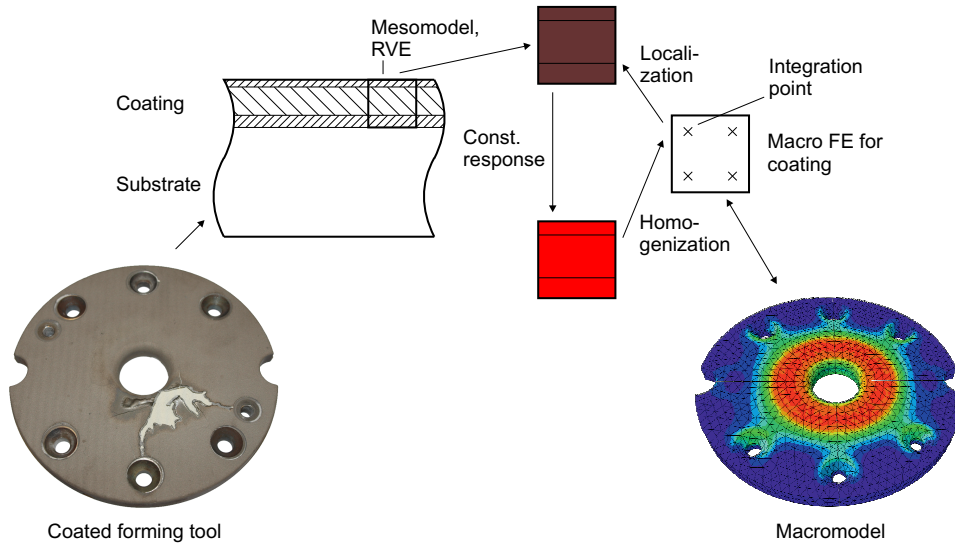


Figure 1: Schematic representation of two scale model

2.1 Macroscopic Thermo-Mechanical Coupled BVP

In a thermo-mechanical coupled problem the basic macroscopic mechanical and thermal variables are the linear strain tensor $\bar{\epsilon}$ and the thermal field vector \bar{m}

$$1. \quad \bar{\epsilon}(\bar{u}) = \text{sym} [\bar{\nabla} \bar{u}(\bar{x})] \quad 2. \quad \bar{m} = \bar{\nabla} \bar{\Theta}(\bar{x}), \quad (1)$$

which are defined by the displacement field \bar{u} , by the position vector \bar{x} and by the temperature $\bar{\Theta}$. In Eq. (1) $\bar{\nabla}$ is the macroscopic gradient operator and in the sequel of the paper $\bar{\nabla} \cdot$ indicates the macroscopic divergence operator. The governing equations are the balance of linear momentum and the balance of energy summarized by

$$1. \quad \bar{\nabla} \cdot \bar{\sigma} + \bar{\rho} \bar{f} = \bar{\rho} \ddot{\bar{u}} \quad 2. \quad \bar{\rho} \bar{r} - \bar{\nabla} \cdot \bar{q} + \bar{\sigma} : \dot{\bar{\epsilon}} = \bar{\rho} \dot{\bar{e}}. \quad (2)$$

In Eq. (2) $\bar{\sigma} = \bar{\sigma}^T$ is the stress tensor, $\bar{\rho}$ is the density, $\bar{\mathbf{f}}$ is the vector of body forces, \bar{r} is a heat source, $\bar{\mathbf{q}}$ is the heat flux vector and \bar{e} is the internal energy. The dot above a scalar, vector or tensor indicates the derivative with respect to time. Mechanical boundary conditions are given in accordance to Figure 2 by

$$1. \bar{\mathbf{u}} = \bar{\mathbf{u}}_b \text{ on } \partial\mathcal{B}_{\bar{\mathbf{u}}} \quad 2. \bar{\mathbf{t}} = \bar{\sigma} \cdot \bar{\mathbf{n}} \text{ on } \partial\mathcal{B}_{\bar{\sigma}}, \quad (3)$$

and thermal boundary conditions yield

$$1. \bar{\Theta} = \bar{\Theta}_b \text{ on } \partial\mathcal{B}_{\bar{\Theta}} \quad 2. \bar{\mathbf{q}} = \bar{\mathbf{q}} \cdot \bar{\mathbf{n}} \text{ on } \partial\mathcal{B}_{\bar{\mathbf{q}}}. \quad (4)$$

Moreover, for the solution of the macroscopic BVP initial conditions must be given, however, not specified in this paper. In a phenomenological macroscopic framework usually a thermodynamic potential is postulated which finally leads to constitutive equations describing the thermo-mechanical behavior of the material of interest. Here, following e.g. Schröder (2009), a representative volume element is attached at each macroscopic integration point $\bar{\mathbf{x}}$, see Figure 3.

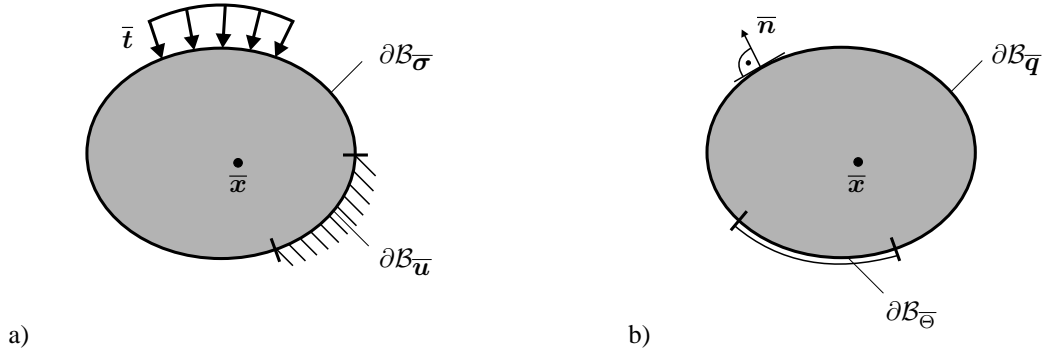


Figure 2: Macroscopic boundary conditions for a) mechanical problem, b) thermal problem

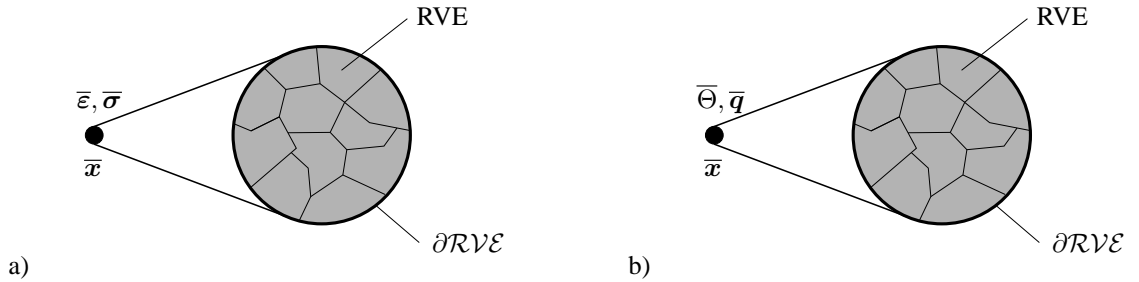


Figure 3: Attached RVE associated to a) mechanical quantities, b) thermal quantities

2.2 Mesoscopic Thermo-Mechanical Coupled BVP

In accordance to the macroscopic BVP on the mesoscale the basic mesoscopic mechanical and thermal variables are the linear strain tensor ε and the thermal field vector \mathbf{m}

$$1. \varepsilon(\mathbf{u}) = \text{sym}[\nabla \mathbf{u}(\mathbf{x})] \quad 2. \mathbf{m} = \nabla \Theta(\mathbf{x}), \quad (5)$$

which are defined by the displacement field \mathbf{u} , by the position vector \mathbf{x} and by the temperature Θ . In Eq. (5) ∇ is the mesoscopic gradient operator and in the sequel of the paper $\nabla \cdot$ indicates the mesoscopic divergence operator. The governing equations are the balance of linear momentum and the balance of energy summarized by

$$1. \nabla \cdot \sigma + \rho \mathbf{f} = \rho \ddot{\mathbf{u}} \quad 2. \rho r - \nabla \cdot \mathbf{q} + \sigma : \dot{\varepsilon} = \rho \dot{e}. \quad (6)$$

In Eq. (6) $\sigma = \sigma^T$ is the stress tensor, ρ is the density, \mathbf{f} is the vector of body forces, r is a heat source, \mathbf{q} is the heat flux vector and e is the internal energy. For the solution of the mesoscopic BVP boundary conditions and initial conditions must be given, however, not specified in this paper. Considering thermodynamic consistent material models on the mesoscale besides the governing equations summarized in Eq. (6) additionally the entropy inequality

$$-\rho \dot{e} + \Theta \rho \dot{\eta} + \sigma : \dot{\varepsilon} - \frac{\mathbf{q} \cdot \mathbf{m}}{\Theta} \geq 0 \quad (7)$$

must be satisfied. Therefore, Eq. (7) is further elaborated in subsection 2.4.

2.3 Scale Transitions

For linking between the macroscopic variables $\{\bar{\varepsilon}, \bar{\sigma}, \bar{\Theta}, \bar{q}\}$ and the mesoscopic variables $\{\varepsilon, \sigma, \Theta, q\}$ a generalized macro-homogeneity condition is postulated, see e.g. Hill (1963); Lee and Sundararaghavan (2009); Maugin (1992); Ostoja-Starzewski (2002); Schröder (2009)

$$\bar{\sigma} : \dot{\bar{\varepsilon}} + \bar{q} \cdot \dot{\bar{m}} = \frac{1}{V} \int_{\text{RVE}} \sigma : \dot{\varepsilon} dV + \frac{1}{V} \int_{\text{RVE}} q \cdot \dot{m} dV. \quad (8)$$

A simple assumption which satisfies Eq. (8) is obtained by setting

$$1. \quad \bar{\sigma} = \sigma = \text{const.} \quad 2. \quad \bar{q} = q = \text{const.} \quad (9)$$

This assumption leads to the so-called Reuss- or Sachs-bounds. Elaborating Eq. (8) leads to

$$\bar{\sigma} : \dot{\bar{\varepsilon}} + \bar{q} \cdot \dot{\bar{m}} = \bar{\sigma} : \frac{1}{V} \int_{\text{RVE}} \dot{\varepsilon} dV + \bar{q} \cdot \frac{1}{V} \int_{\text{RVE}} \dot{m} dV \quad (10)$$

and finally to

$$1. \quad \bar{\varepsilon} = \frac{1}{V} \int_{\text{RVE}} \varepsilon dV \quad 2. \quad \bar{m} = \frac{1}{V} \int_{\text{RVE}} m dV. \quad (11)$$

Alternatively, another simple assumption which satisfies Eq. (8) is obtained by setting

$$1. \quad \bar{\varepsilon} = \varepsilon = \text{const.} \quad 2. \quad \bar{m} = m = \text{const.} \quad (12)$$

This assumption leads to the so-called Voigt- or Taylor-bounds. Elaborating Eq. (8) leads to

$$\bar{\sigma} : \dot{\bar{\varepsilon}} + \bar{q} \cdot \dot{\bar{m}} = \frac{1}{V} \int_{\text{RVE}} \sigma dV : \dot{\bar{\varepsilon}} + \frac{1}{V} \int_{\text{RVE}} q dV \cdot \dot{\bar{m}} \quad (13)$$

and finally to

$$1. \quad \bar{\sigma} = \frac{1}{V} \int_{\text{RVE}} \sigma dV \quad 2. \quad \bar{q} = \frac{1}{V} \int_{\text{RVE}} q dV. \quad (14)$$

In addition to the above two assumptions of course different kinds of boundary condition can be applied, for example periodic boundary conditions, see e.g. Suquet (1985).

2.4 Mesoscopic Entropy Inequality

In order to get a thermodynamically consistent model, we proceed with the Clausius-Duhem inequality (7) on the mesoscale. Using the well-known Legendre-transformation between the internal energy e and the Helmholtz free energy Ψ

$$\Psi = e - \Theta \eta \quad (15)$$

the Clausius-Duhem inequality (7) becomes

$$\frac{1}{\rho} \sigma : \dot{\varepsilon} - \dot{\Psi} - \eta \dot{\Theta} - \frac{q \cdot m}{\rho \Theta} \geq 0. \quad (16)$$

Let the Helmholtz free energy be given by

$$\Psi = \Psi[\varepsilon^{el}, \mathbf{V}_i, \Theta], \quad (17)$$

where \mathbf{V}_i is a vector of scalar and tensorial hardening internal variables of strain type. Then, using the additive decomposition of the strain tensor $\varepsilon = \varepsilon^{el} + \varepsilon^{in}$ considering an elastic part ε^{el} and an inelastic part ε^{in} the Clausius-Duhem inequality results into

$$\frac{\sigma}{\rho} : \dot{\varepsilon}^{in} - \left(\frac{\partial \Psi}{\partial \varepsilon^{el}} - \frac{\sigma}{\rho} \right) : \dot{\varepsilon}^{el} - \left(\frac{\partial \Psi}{\partial \Theta} + \eta \right) \dot{\Theta} - \frac{\partial \Psi}{\partial \mathbf{V}_i} : \dot{\mathbf{V}}_i - \frac{q \cdot m}{\rho \Theta} \geq 0. \quad (18)$$

By standard arguments (Truesdell and Noll, 1965) the following potential relations result from Eq. (18)

$$1. \quad \boldsymbol{\sigma} = \rho \frac{\partial \Psi}{\partial \boldsymbol{\varepsilon}^{el}}, \quad 2. \quad \eta = -\frac{\partial \Psi}{\partial \Theta}. \quad (19)$$

In this way $\boldsymbol{\sigma}$ and η can be regarded as thermodynamical forces. Next, considering isotropic and kinematic hardening, by introduction of the hardening internal variables α and $\boldsymbol{\beta}$ for \mathbf{V}_i we define further thermodynamical forces by

$$1. \quad R = \rho \frac{\partial \Psi}{\partial \alpha}, \quad 2. \quad \mathbf{X} = \rho \frac{\partial \Psi}{\partial \boldsymbol{\beta}}. \quad (20)$$

In Eq. (20) R is the isotropic hardening stress and \mathbf{X} is the kinematic hardening stress tensor. Then, with dissipative terms

$$1. \quad \mathcal{D}^i = \boldsymbol{\sigma} : \dot{\boldsymbol{\varepsilon}}^{in} - R\dot{\alpha} - \mathbf{X} : \dot{\boldsymbol{\beta}}, \quad 2. \quad \mathcal{D}^\Theta = -\frac{1}{\Theta} \mathbf{q} \cdot \mathbf{m} \quad (21)$$

the Clausius-Duhem inequality (18) is rewritten as

$$\mathcal{D}^i + \mathcal{D}^\Theta \geq 0. \quad (22)$$

A stronger condition of this inequality is introduced by setting both parts greater than zero, which results into

$$\begin{aligned} 1. \quad & \text{Clausius-Planck inequality: } \mathcal{D}^i \geq 0 \\ 2. \quad & \text{Heat conduction inequality: } \mathcal{D}^\Theta \geq 0. \end{aligned} \quad (23)$$

A common approach for the heat flux vector in Eq. (21.2) is given by Fourier's law

$$\mathbf{q} = -\lambda^{th} \mathbf{m}, \quad (24)$$

with λ^{th} being a non-negative heat conduction coefficient. Consequently, the heat conduction inequality is satisfied.

In a general setting it becomes necessary to formulate evolution equations

$$\begin{aligned} 1. \quad \dot{\boldsymbol{\varepsilon}}^{in} &= \dot{\boldsymbol{\varepsilon}}^{in}[\boldsymbol{\sigma}, R, \mathbf{X}, \boldsymbol{\varepsilon}^{in}, \alpha, \boldsymbol{\beta}, \Theta] \\ 2. \quad \dot{\alpha} &= \dot{\alpha}[\boldsymbol{\sigma}, R, \mathbf{X}, \boldsymbol{\varepsilon}^{in}, \alpha, \boldsymbol{\beta}, \Theta] \\ 3. \quad \dot{\boldsymbol{\beta}} &= \dot{\boldsymbol{\beta}}[\boldsymbol{\sigma}, R, \mathbf{X}, \boldsymbol{\varepsilon}^{in}, \alpha, \boldsymbol{\beta}, \Theta] \end{aligned} \quad (25)$$

which are in accordance with the Clausius-Planck inequality (23.1), such that the model under consideration becomes thermodynamically consistent. In this work the evolution equations (25) are briefly summarized in the next subsection. For more thermodynamic background see e.g. Chaboche (1997); Mahnken and Schlimmer (2005); Mahnken (2010).

2.5 Mesoscopic Heat Conduction Equation

The heat conduction equation can be derived in a standard way from the energy equation (6.2). Taking into account Eq. (15), (17), (19) and (20) yields

$$\nabla \cdot \mathbf{q} = \boldsymbol{\sigma} : \dot{\boldsymbol{\varepsilon}} + \rho r - \rho \dot{\Theta} \eta - \rho \Theta \dot{\eta} - \boldsymbol{\sigma} : \dot{\boldsymbol{\varepsilon}}^{el} - R\dot{\alpha} - \mathbf{X} : \dot{\boldsymbol{\beta}} + \rho \dot{\Theta} \eta. \quad (26)$$

Finally, using the resulting relation from (19.2) and (17)

$$\rho \dot{\eta} = -\frac{\partial \boldsymbol{\sigma}}{\partial \Theta} : \dot{\boldsymbol{\varepsilon}}^{el} - \frac{\partial R}{\partial \Theta} \dot{\alpha} - \frac{\partial \mathbf{X}}{\partial \Theta} : \dot{\boldsymbol{\beta}} - \rho \frac{\partial^2 \Psi}{\partial \Theta^2} \dot{\Theta}, \quad (27)$$

one gets the heat conduction equation

$$\rho c_p \dot{\Theta} + \nabla \cdot \mathbf{q} = \boldsymbol{\sigma} : \dot{\boldsymbol{\varepsilon}}^{in} - R\dot{\alpha} - \mathbf{X} : \dot{\boldsymbol{\beta}} + \Theta \frac{\partial \boldsymbol{\sigma}}{\partial \Theta} : \dot{\boldsymbol{\varepsilon}}^{el} + \Theta \frac{\partial R}{\partial \Theta} \dot{\alpha} + \Theta \frac{\partial \mathbf{X}}{\partial \Theta} : \dot{\boldsymbol{\beta}} + \rho r \quad (28)$$

with the heat capacity

$$c_p = -\Theta \frac{\partial^2 \Psi}{\partial \Theta^2}. \quad (29)$$

2.6 Derivation of Macroscopic Heat Conduction Equation

The macroscopic heat conduction equation is derived by homogenization of Eq. (28), thus leading to

$$\begin{aligned} \frac{1}{V} \int_{\text{RVE}} \rho c_p \dot{\Theta} dV + \frac{1}{V} \int_{\text{RVE}} \nabla \cdot \mathbf{q} dV &= \frac{1}{V} \int_{\text{RVE}} \boldsymbol{\sigma} : \dot{\boldsymbol{\varepsilon}}^{in} dV - \frac{1}{V} \int_{\text{RVE}} R \dot{\alpha} dV - \frac{1}{V} \int_{\text{RVE}} \mathbf{X} : \dot{\boldsymbol{\beta}} dV \\ &+ \frac{1}{V} \int_{\text{RVE}} \Theta \frac{\partial \boldsymbol{\sigma}}{\partial \Theta} : \dot{\boldsymbol{\varepsilon}}^{el} dV + \frac{1}{V} \int_{\text{RVE}} \Theta \frac{\partial R}{\partial \Theta} \dot{\alpha} dV + \frac{1}{V} \int_{\text{RVE}} \Theta \frac{\partial \mathbf{X}}{\partial \Theta} : \dot{\boldsymbol{\beta}} dV + \frac{1}{V} \int_{\text{RVE}} \rho r dV. \end{aligned} \quad (30)$$

Applying Eq. (12.1) and (14) and the definitions for the macroscopic heat source $\overline{\rho r}$ and for the macroscopic internal energy $\overline{\rho e}$ (Maugin, 1992)

$$\begin{aligned} 1. \quad \overline{\rho r} &=: \frac{1}{V} \int_{\text{RVE}} \rho r dV & 2. \quad \overline{\rho e} &=: \frac{1}{V} \int_{\text{RVE}} \rho e dV & 3. \quad \overline{\rho} &=: \frac{1}{V} \int_{\text{RVE}} \rho dV \end{aligned} \quad (31)$$

yields

$$\begin{aligned} \overline{\rho \dot{e}} + \nabla \cdot \overline{\mathbf{q}} &= \overline{\boldsymbol{\sigma}} : \dot{\boldsymbol{\varepsilon}}^{in} - \frac{1}{V} \int_{\text{RVE}} R \dot{\alpha} dV - \frac{1}{V} \int_{\text{RVE}} \mathbf{X} : \dot{\boldsymbol{\beta}} dV \\ &+ \frac{1}{V} \int_{\text{RVE}} \Theta \frac{\partial \boldsymbol{\sigma}}{\partial \Theta} : \dot{\boldsymbol{\varepsilon}}^{el} dV + \frac{1}{V} \int_{\text{RVE}} \Theta \frac{\partial R}{\partial \Theta} \dot{\alpha} dV + \frac{1}{V} \int_{\text{RVE}} \Theta \frac{\partial \mathbf{X}}{\partial \Theta} : \dot{\boldsymbol{\beta}} dV + \overline{\rho r}. \end{aligned} \quad (32)$$

Using the definitions for the macroscopic isotropic and kinematic dissipative terms

$$\begin{aligned} 1. \quad \overline{R \dot{\alpha}} &=: \frac{1}{V} \int_{\text{RVE}} R \dot{\alpha} dV & 2. \quad \overline{\mathbf{X} : \dot{\boldsymbol{\beta}}} &=: \frac{1}{V} \int_{\text{RVE}} \mathbf{X} : \dot{\boldsymbol{\beta}} dV \end{aligned} \quad (33)$$

and the definitions for the macroscopic thermo-mechanical coupling parts

$$\begin{aligned} 1. \quad \overline{\Theta \frac{\partial \boldsymbol{\sigma}}{\partial \Theta} : \dot{\boldsymbol{\varepsilon}}^{el}} &=: \frac{1}{V} \int_{\text{RVE}} \Theta \frac{\partial \boldsymbol{\sigma}}{\partial \Theta} : \dot{\boldsymbol{\varepsilon}}^{el} dV \\ 2. \quad \overline{\Theta \frac{\partial R}{\partial \Theta} \dot{\alpha}} &=: \frac{1}{V} \int_{\text{RVE}} \Theta \frac{\partial R}{\partial \Theta} \dot{\alpha} dV \\ 3. \quad \overline{\Theta \frac{\partial \mathbf{X}}{\partial \Theta} : \dot{\boldsymbol{\beta}}} &=: \frac{1}{V} \int_{\text{RVE}} \Theta \frac{\partial \mathbf{X}}{\partial \Theta} : \dot{\boldsymbol{\beta}} dV \end{aligned} \quad (34)$$

finally leads to the macroscopic heat conduction equation

$$\overline{\rho \dot{e}} + \nabla \cdot \overline{\mathbf{q}} = \overline{\boldsymbol{\sigma}} : \dot{\boldsymbol{\varepsilon}}^{in} - \overline{R \dot{\alpha}} - \overline{\mathbf{X} : \dot{\boldsymbol{\beta}}} + \overline{\Theta \frac{\partial \boldsymbol{\sigma}}{\partial \Theta} : \dot{\boldsymbol{\varepsilon}}^{el}} + \overline{\Theta \frac{\partial R}{\partial \Theta} \dot{\alpha}} + \overline{\Theta \frac{\partial \mathbf{X}}{\partial \Theta} : \dot{\boldsymbol{\beta}}} + \overline{\rho r}. \quad (35)$$

2.7 Constitutive Equations on Mesoscale

Within the applied multiscale model the constitutive equations are formulated on the mesoscale leading to possible different material models for different layers of the coating system shown in Figure 1. Therefore, the following subsections summarize briefly the material models being applied in the latter numerical examples.

2.7.1 Thermo-Elastic Material Model

The most simple material model applied in this work is a thermo-elastic material model. Thermo-elastic material behavior is summarized by

1. $\Psi = \Psi^{el} + \Psi^{th} = \frac{1}{2\rho} \boldsymbol{\varepsilon}^{el} : \mathbf{C}^{el} : \boldsymbol{\varepsilon}^{el} - \frac{1}{\rho} \boldsymbol{\varepsilon}^{el} : \mathbf{C}^{el} : \boldsymbol{\varepsilon}^{th}$
2. $\boldsymbol{\varepsilon} = \boldsymbol{\varepsilon}^{el} + \boldsymbol{\varepsilon}^{th}, \quad \boldsymbol{\varepsilon}^{th} = \alpha^{th} \Theta \mathbf{1}$
3. $\boldsymbol{\sigma} = \mathbf{C}^{el} : (\boldsymbol{\varepsilon}^{el} - \boldsymbol{\varepsilon}^{th})$
4. $\mathbf{C}^{el} = K \mathbf{1} \otimes \mathbf{1} + 2G \mathbf{I}^{dev}$
5. $\boldsymbol{\kappa}^{el} = [G, K, \alpha^{th}]$.

(36)

Eq. (36.1) states Helmholtz free energy and Eq. (36.2) yields the additive decomposition of the total strain tensor using the elastic strain tensor and the thermal expansion strain tensor $\boldsymbol{\varepsilon}^{th}$. Further, Eq. (36.3) defines the stress tensor following (19.1), Eq. (36.4) constitutes the elasticity tensor \mathbf{C}^{el} using the second-order unit tensor $\mathbf{1}$ and the deviatoric part of the fourth-order unit tensor \mathbf{I}^{dev} and Eq. (36.5) summarizes the material parameters, in particular the shear modulus G , the bulk modulus K and the coefficient of thermal expansion α^{th} .

2.7.2 Thermo-Elasto-Viscoplastic Material Model

The thermo-elasto-viscoplastic material model is an extension of the thermo-elastic material model. Thermo-elasto-viscoplastic material behavior is summarized by

1. $\Psi = \Psi^{el} + \Psi^{vp} + \Psi^{th} = \frac{1}{2\rho} \boldsymbol{\varepsilon}^{el} : \mathbf{C}^{el} : \boldsymbol{\varepsilon}^{el} + \frac{1}{2\rho} (H_3 \alpha^2 + H_1 \boldsymbol{\beta} : \boldsymbol{\beta}) - \frac{1}{\rho} \boldsymbol{\varepsilon}^{el} : \mathbf{C}^{el} : \boldsymbol{\varepsilon}^{th}$
2. $\boldsymbol{\varepsilon} = \boldsymbol{\varepsilon}^{el} + \boldsymbol{\varepsilon}^{vp} + \boldsymbol{\varepsilon}^{th}, \quad \boldsymbol{\varepsilon}^{th} = \alpha^{th} \Theta \mathbf{1}$
3. $\boldsymbol{\sigma} = \mathbf{C}^{el} : (\boldsymbol{\varepsilon}^{el} - \boldsymbol{\varepsilon}^{th}), \quad \mathbf{X} = H_1 \boldsymbol{\beta}, \quad R = H_3 \alpha$
4. $\dot{\boldsymbol{\varepsilon}}^{vp} = \frac{3}{2} \gamma \mathbf{n}, \quad \mathbf{n} = \frac{\boldsymbol{\sigma}^{dev} - \mathbf{X}}{\|\boldsymbol{\sigma}^{dev} - \mathbf{X}\|}$
5. $\Phi = \sqrt{\frac{3}{2}} \|\boldsymbol{\sigma}^{dev} - \mathbf{X}\| - R - Y_0, \quad \Phi^* = \Phi + \frac{H_4}{2H_3} R^2 + \frac{H_2}{2H_1} \mathbf{X} : \mathbf{X}$
6. $\gamma = \left\langle \frac{\Phi}{K_\lambda} \right\rangle^m$
7. $\dot{\mathbf{X}} = H_1 \dot{\boldsymbol{\varepsilon}}^{vp} - H_2 \mathbf{X} \gamma, \quad \dot{R} = H_3 \gamma - H_4 R \gamma$
8. $\boldsymbol{\kappa}^{vp} = [G, K, Y_0, K_\lambda, m, H_1, H_2, H_3, H_4, \alpha^{th}]$

(37)

In addition to the thermo-elastic material model Eq. (37.3) defines further thermodynamical forces \mathbf{X} and R . Eq. (37.4) constitutes the flow rule using the flow factor γ and the flow direction \mathbf{n} defined by the deviatoric part of the stress tensor $\boldsymbol{\sigma}^{dev}$ and by the back stress tensor \mathbf{X} . Further, Eq. (37.5) yields the overstress function Φ considering a von Mises type flow condition and the plastic potential Φ^* . The flow factor is obtained by Eq. (37.6), Eq. (37.7) represents the evolution equations for kinematic and isotropic hardening stresses and Eq. (37.8) summarizes the material parameters, in particular the yield strength Y_0 , K_λ and m related to rate-dependency, H_1 and H_2 related to kinematic hardening and H_3 and H_4 related to isotropic hardening.

2.7.3 Thermo-Elasto-Viscoplastic Material Model with Damage

The thermo-elasto-viscoplastic material model with damage is an advanced thermo-elasto-viscoplastic material model, which was originally applied for the simulation of strength difference effects in elasto-plasticity for adhesive

materials (Mahnken and Schlimmer, 2005; Mahnken, 2010). Within this framework

1. $\Psi = \Psi^{el} + \Psi^{vp} + \Psi^{th} = \frac{1}{2\rho} \boldsymbol{\varepsilon}^{el} : \mathbf{C}^{el} : \boldsymbol{\varepsilon}^{el} + \frac{q}{\rho} \left(e_v + \frac{1}{b} e^{-be_v} \right) + \frac{1}{2\rho} H e_v^2 - \frac{1}{\rho} \boldsymbol{\varepsilon}^{el} : \mathbf{C}^{el} : \boldsymbol{\varepsilon}^{th}$
2. $\boldsymbol{\varepsilon} = \boldsymbol{\varepsilon}^{el} + \boldsymbol{\varepsilon}^{vp} + \boldsymbol{\varepsilon}^{th}, \quad \boldsymbol{\varepsilon}^{th} = \alpha^{th} \Theta \mathbf{1}$
3. $\boldsymbol{\sigma} = \mathbf{C}^{el} : (\boldsymbol{\varepsilon}^{el} - \boldsymbol{\varepsilon}^{th})$

(38)

describes Helmholtz free energy, the concept of additive decomposition of the strain tensor for a geometrical linear theory as well as thermo-elastic material behavior. Furthermore,

1. $\Phi = J_2^{eff} - \frac{1}{3} \varphi$
2. $\varphi = Y^2 - a_1 Y_0 I_1^{eff} - a_2 (I_1^{eff})^2$
3. $I_1^{eff} = \frac{I_1}{W}, \quad J_2^{eff} = \frac{J_2}{W}$
4. $I_1 = \mathbf{1} : \boldsymbol{\sigma}, \quad J_2 = \frac{1}{2} \mathbf{1} : (\boldsymbol{\sigma}^{dev})^2$
5. $Y = Y_0 + R(e_v)$
6. $R(e_v) = q(1 - e^{-be_v}) + H e_v$

(39)

defines the yield function Φ , which depends on the first invariant of the stress tensor I_1 , on the second invariant of the deviatoric stress tensor J_2 , on an isotropic hardening stress R driven by a strain-like internal variable e_v and on an independent scalar damage variable W . In order to account for a non-associative flow rule, additionally a plastic potential is introduced by

1. $\Phi^* = J_2 - \frac{1}{3} \varphi^*$
2. $\varphi^* = Y^2 - a_1^* Y_0 I_1 - a_2^* I_1^2$

(40)

with the same mathematical structure as the yield function. For evolution of the viscoplastic strain tensor, the rate equation given by

1. $\dot{\boldsymbol{\varepsilon}}^{vp} = \gamma \frac{\partial \Phi^*}{\partial \boldsymbol{\sigma}} = \gamma \boldsymbol{\sigma}^{dev} + \gamma g \mathbf{1}$
2. $g = \frac{1}{3} (a_1^* Y_0 + 2a_2^* I_1)$

(41)

is derived from the plastic potential. Additionally, the plastic multiplier is obtained from

$$\gamma = K_\lambda \langle \Phi \rangle^m. \quad (42)$$

In order to formulate a rate equation for the strain-like internal variable e_v the expression of equivalence of dissipated power as constituted by

$$\dot{e}_v Y = \boldsymbol{\sigma} : \boldsymbol{\varepsilon}^{vp} \Rightarrow \dot{e}_v = \frac{1}{Y} \boldsymbol{\sigma} : \boldsymbol{\varepsilon}^{vp} = \frac{\gamma}{Y} (g I_1 + 2J_2) \quad (43)$$

is postulated. This leads to an additive decomposition of the strain-like internal variable according to

$$\dot{e}_v = \dot{e}_v^{vol} + \dot{e}_v^{dev} = \frac{\gamma}{Y} g I_1 + 2 \frac{\gamma}{Y} J_2. \quad (44)$$

The independent scalar damage variable W is decomposed multiplicatively according to

$$W = W^{vol} \cdot W^{dev}. \quad (45)$$

The undamaged case is described by $W = 1$ and the damaged case is described by $W = 0$. The deviatoric part is postulated considering

$$W^{dev} = \begin{cases} 1, & \text{if } e_v^{dev} \leq e^{dev} \\ \exp(*w^{dev} (e^{dev} - e_v^{dev})^{n^{dev}}), & \text{if } e_v^{dev} > e^{dev} \end{cases} \quad (46)$$

where e^{dev} is a threshold value and n^{dev} is an exponent. Using the additional material parameters w^{dev} and d^{dev} an additional scalar damage value is introduced by

$${}^*w^{dev} = \begin{cases} \frac{e_v^{dev} - e^{dev}}{d^{dev}} w^{dev}, & \text{if } e_v^{dev} \leq e^{dev} + d^{dev} \\ w^{dev}, & \text{if } e_v^{dev} > e^{dev} + d^{dev} \end{cases}. \quad (47)$$

Analogously, volumetric softening is introduced according to

$$W^{vol} = \begin{cases} 1, & \text{if } e_v^{vol} \leq e^{vol} \\ \exp({}^*w^{vol}(e^{vol} - e_v^{vol})n^{vol}), & \text{if } e_v^{vol} > e^{vol} \end{cases} \quad (48)$$

with

$${}^*w^{vol} = \begin{cases} \frac{e_v^{vol} - e^{vol}}{d^{vol}} w^{vol}, & \text{if } e_v^{vol} \leq e^{vol} + d^{vol} \\ w^{vol}, & \text{if } e_v^{vol} > e^{vol} + d^{vol} \end{cases}. \quad (49)$$

Furthermore, another dependent damage variable is introduced by

$$D = 1 - W. \quad (50)$$

Finally, the vector of material parameters is given by

$$\boldsymbol{\kappa}^{vpd} = [G, K, Y_0, H, b, q, a_1, a_1^*, a_2, a_2^*, K_\lambda, m, e^{dev}, w^{dev}, d^{dev}, n^{dev}, e^{vol}, w^{vol}, d^{vol}, n^{vol}, \alpha^{th}]. \quad (51)$$

2.8 Remarks on Thermal Material Model

For all layer materials and for the substrate of the forming tool the thermal constitutive material model considers Fourier heat conduction, see Eq. (24). For implicit calculations using the elasto-viscoplastic material model with damage for one or more specific layers of the coating system the dependent damage variable D is incorporated into the thermal constitutive model with respect of simulating a modified heat flux through a partially damaged coating layer. This idea is adopted from Özdemir et al. (2010), who model a reduction in effective conductivity resulting from a partially open cohesive crack. In our work the implementation considers a reduced volume of the damaged layer according to

$$V^{red} = (1 - D)^2 \cdot V \quad (52)$$

leading to a reduced influence of the damaged layer on the homogenization process of the macroscopic heat flux.

3 Remarks on Numerical Implementation

This section briefly illustrates the implementation of the two scale finite element model for numerical simulation of coated hybrid forming tools using an implicit solution strategy. The two scale model is defined using the umat-interface of the commercial finite element software Abaqus/Standard.

Following standard integration procedures in finite element techniques a strain-driven algorithm is considered, where the total strain ${}^{n+1}\boldsymbol{\varepsilon}$ and initial values ${}^n\varepsilon^{vp}, {}^n\gamma, {}^n e_v$ are given at each time step ${}^n t$. Then it is the object to find the corresponding quantities ${}^{n+1}\varepsilon^{vp}, {}^{n+1}\gamma, {}^{n+1} e_v$ at time ${}^{n+1} t$ consistent with the respective constitutive equations and to update the stresses ${}^{n+1}\boldsymbol{\sigma}$. Additionally, the algorithmic tangent moduli ${}^{n+1}\mathbf{C} = \partial\boldsymbol{\sigma}/\partial\boldsymbol{\varepsilon}$ must be updated for application of a Newton method for iterative solution of the global equilibrium problem on the mesolevel. A detailed description of the applied integration schemes for the particular material models is given in Mahnken (1999); Mahnken and Schlimmer (2005); Mahnken (2010) and therefore will not be elaborated further in this paper.

After updating the stresses, history variables and the algorithmic tangent moduli on the mesolevel their macroscopic counterparts are calculated using Eq. (14.1) at time ${}^{n+1} t$ for ${}^{n+1}\bar{\boldsymbol{\sigma}}$ and

$$\bar{\mathbf{C}} = \frac{1}{V} \int_{\text{RVE}} \mathbf{C} dV \quad (53)$$

at time $n+1t$ for $n+1\bar{C}$. Due to the quite simple geometry of the RVE shown in Figure 4 the stresses and the algorithmic tangent modulus on macro level are finally calculated by

$$1. \bar{\sigma} = \frac{1}{H} \sum_{i=1}^{n_L} h_i \sigma, \quad 2. \bar{C} = \frac{1}{H} \sum_{i=1}^{n_L} h_i C. \quad (54)$$

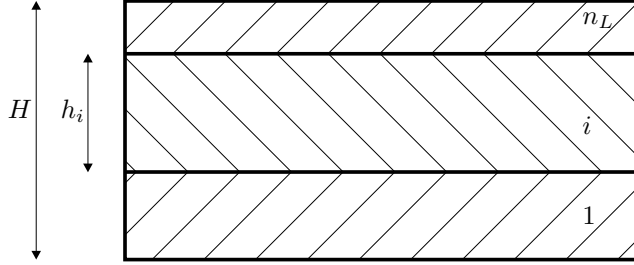


Figure 4: Representative volume element of coating system

Here it should be remarked that within the applied finite element code the material parameters $\{\alpha^{th}, \rho, \lambda^{th}, c_p\}$ can only be specified in terms of their macroscopic counterparts $\{\bar{\alpha}^{th}, \bar{\rho}, \bar{\lambda}^{th}, \bar{c}_p\}$, except for $\{\lambda^{th}, c_p\}$ when simulating the modified heat flux through a partially damaged coating layer for implicit calculations. This leads to the restrictions

$$\begin{aligned} 1. \alpha^{th} &= \bar{\alpha}^{th} = \text{const.} & 2. \rho &= \bar{\rho} = \text{const.} \\ 3. \lambda^{th} &= \bar{\lambda}^{th} = \text{const.} & 4. c_p &= \bar{c}_p = \text{const.} \end{aligned} \quad (55)$$

4 Numerical Examples

The ensuing subsections show two numerical examples with application of the two scale approach for coated forming tools onto the coating elements. In the applied two scale approach the Taylor-assumption (12) is used. The coating system of the coated forming tool under investigation consists of a metallic NiCr layer and a porous ceramic Al_2O_3 layer applied by thermal spraying, and finally a Cr-CrAlN layer is applied using physical vapor deposition. Since no experimental data for the layer materials are available up to now in the numerical examples artificial material parameters are utilized. Nevertheless, the elasto-viscoplastic material model with damage is applied with respect to simulate the material behavior of the porous ceramic layer.

The first example uses an implicit solution strategy due to model the modified heat flux through a partially damaged coating layer using an additional user-subroutine for the thermal constitutive behavior. The second example uses an explicit solution strategy due to model coating failure by element deletion caused by a damaged coating layer using a user-defined element deletion criterion.

Here it should be remarked that the dissipative terms and the thermo-mechanical coupling terms in the heat conduction equation (28) are neglected in the numerical examples. Moreover internal heat sources are disregarded on the mesoscale, thus leading to the resulting heat conduction equation

$$-\nabla \cdot (-\lambda^{th} \nabla \Theta) = \rho c_p \dot{\Theta}. \quad (56)$$

Due to the neglect of the thermo-mechanical coupling terms a staggered solution strategy is applied. Within this strategy first the thermal problem is solved for a small temperature increment and then the mechanical solution is updated.

4.1 Coated Steel Volume Element

The example model consists of a viscoplastic steel substrate with a coating system built-up of three coating layers. The steel substrate is a cube with a side length of 10 mm for each lateral side and a height of 9 mm (see Figure 5). The coating system is a rectangular plate with a side length of 10 mm for each lateral side and a thickness of 1 mm.

On the mesolevel, the coating system is built-up of an elastic layer, a viscoplastic layer and a viscoplastic layer with damage. The individual layer thicknesses are 0.3 mm, 0.1 mm and 0.6 mm, respectively. Since the Taylor assumption is applied in the two scale model the order of the layers has no influence on the numerical results. The mechanical material parameters are summarized according to Table 1. The first line states the mechanical material parameters used for the substrate and the subsequent lines state the mechanical parameters used for the coating layers. Since thermal expansion strains are not considered in this example the values for the coefficients of thermal expansion are omitted in Table 1. For the substrate and for the coating the density is chosen constant with $7\,850\text{ kg/m}^3$. Further, for the substrate the conductivity is chosen constant with 25 W/mK and specific heat is chosen constant with 460 J/kgK . The individual layer conductivities are 25 W/mK for the elastic and viscoplastic layer and 1 W/mK for the viscoplastic layer with damage indicating that this layer should represent a thermal barrier layer (TBL). For all layer materials specific heat is chosen constant with 460 J/kgK . The simulation is carried out twice with two different sets of parameters for the damage model of the TBL. If damage parameter set *A* is used damage is not activated in this example and if damage parameter set *B* is used damage is activated in this example. For connection between the substrate element and the coating element a tie constraint is applied. In the implicit thermo-mechanical coupled simulation two loading steps are applied, first a mechanical loading step for 1 s for possible damage activation in the TBL and then a thermal loading step for 9 s for investigation of possible different heat fluxes through the coating system with and without damage activation in the TBL. According to Figure 5 the mechanical loading is realized by a predetermined displacement of 1.2 mm of the top surface of the coating element, while the bottom surface of the substrate and all vertical surfaces of the substrate and of the coating are fixed in normal directions. The thermal loading is realized by a predetermined surface temperature of the top surface of the coating element of $1\,000\text{ }^\circ\text{C}$, while the starting temperature of the whole model is $20\text{ }^\circ\text{C}$. The substrate and the coating are discretized each with one standard hexahedral element with linear geometric order and with thermal and mechanical degrees of freedom (C3D8T).

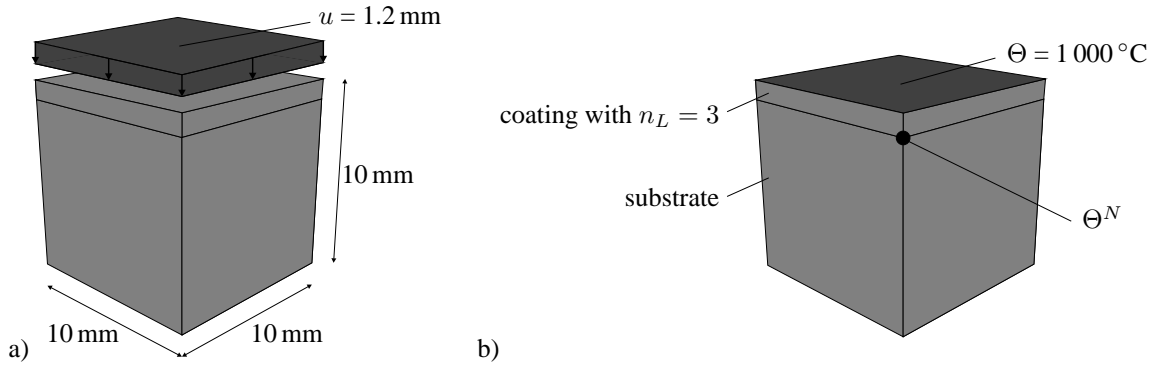


Figure 5: Coated steel volume element, a) geometry and mechanical loading, b) thermal loading (on boundary conditions see text)

Table 1: Steel volume element: mechanical material parameters with damage parameter set *B*

κ^{vp} :	G [MPa]	K [MPa]	Y_0 [MPa]	K_λ [MPa]	m [-]	H_1 [MPa]	H_2 [MPa]	H_3 [MPa]	H_4 [MPa]
	80 769	175 000	930	10^{-9}	2	73 393	128	-28 261	128
κ^{el} :	G [MPa]	K [MPa]							
	83 076	180 000							
κ^{vp} :	G [MPa]	K [MPa]	Y_0 [MPa]	K_λ [MPa]	m [-]	H_1 [MPa]	H_2 [MPa]	H_3 [MPa]	H_4 [MPa]
	80 769	175 000	930	10^{-9}	2	73 393	128	-28 261	128
κ^{vpd} :	G [MPa]	K [MPa]	Y_0 [MPa]	H [MPa]	b [-]	q [MPa]	a_1 [-]	a_1^* [-]	a_2 [-]
	69 231	150 000	400	800	3	500	0.2	0.2	0.3
	a_2^* [-]	K_λ [MPa]	m [-]	e^{dev} [-]	w^{dev} [-]	d^{dev} [-]	n^{dev} [-]	e^{vol} [-]	w^{vol} [-]
	0.3	10^{-9}	2	0.002	2 000	10^{-9}	3	0.002	2 000
	d^{vol} [-]	n^{vol} [-]							
	10^{-9}	3							

Results of the two simulations with and without damage activation are illustrated according to Figure 6. Figure 6 a) shows increasing values of the volumetric and deviatoric parts of the internal strain-like variable of the TBL leading to increasing values of the volumetric and deviatoric parts of the dependent damage variable D for the simulation with damage activation using damage parameter set B . Finally, the dependent damage variable D reaches values of over 90 % at the end of the simulation. Additionally, Figure 6 b) compares the macroscopic temperature evolution at position Θ_N introduced in Figure 5 b) with and without activation of mesoscopic damage in the TBL. Without damage activation the maximum temperature reads 720 °C at the end of the simulation and with damage activation the maximum temperature reads 870 °C at the end of the simulation. To summarize, damage of the TBL leads to higher temperatures in the substrate.

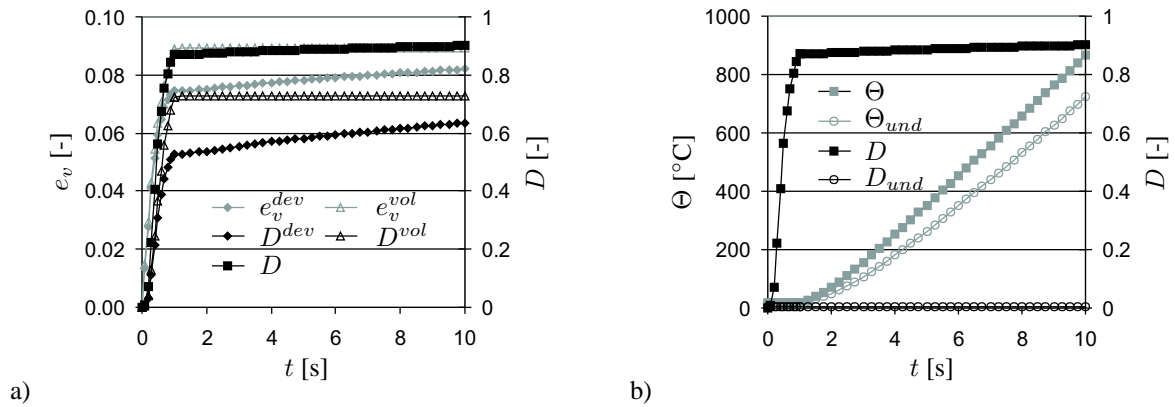


Figure 6: Steel volume element, a) internal variable e_v and dependent damage variable D of TBL with damage activation, b) macroscopic temperature evolution at Θ_N with and without damage activation

4.2 Coated Hybrid Forming Tool

The example model consists of an elastic substrate with a coating system built-up of two coating layers. The geometries of the substrate and the coating are illustrated in Figure 7. The substrate has a thickness of 9 mm and the coating has a thickness of 1 mm. On the mesolevel, the coating system is built-up of an elastic layer and a viscoplastic layer with damage. The individual layer thicknesses are 0.2 mm and 0.8 mm, respectively. The mechanical material parameters are summarized according to Table 2. The first line states the mechanical material parameters used for the substrate and the subsequent lines state the mechanical parameters used for the coating layers. The parameters for the damage model of the viscoplastic layer with damage are chosen in a way that there is damage activation in the example model. For the substrate and for the coating the density is chosen constant with 7850 kg/m³, the conductivity is chosen constant with 25 W/mK and specific heat is chosen constant with 460 J/kgK. For connection between substrate and coating a tie constraint is applied. In the explicit thermo-mechanical coupled simulation two loading steps are applied, first a thermo-mechanical loading step for 1 s and then another thermo-mechanical loading step for 1 s. Since this example is quasi-static, a constant mass scaling factor $f = 1000$ is applied to the whole model for both loading steps due to decrease the calculation time. According to Figure 7 b) the mechanical loading is realized by a homogeneous predetermined pressure of 400 MPa applied to the light grey and dark grey region on the forming surface in the first loading step. In the second loading step a pressure of 600 MPa is predetermined on the dark grey region indicating inhomogeneous mechanical loading conditions. Additionally, according to Figure 7 b) the thermal loading is realized by a homogeneous predetermined temperature of 400 °C applied to the light grey and dark grey region on the forming surface in the first loading step. In the second loading step a temperature of 600 °C is predetermined on the dark grey region indicating inhomogeneous thermal loading conditions. Aiming to achieve a realistic bearing the bottom surface of the substrate is fixed in normal direction. The starting temperature of the whole model is 20 °C. Furthermore, in this explicit calculation a user-defined element deletion criterion is applied. Elements are deleted, if the dependent damage variable D exceeds 60 %. The substrate is discretized with 11 880 hexahedral standard elements with linear geometric order and with thermal and mechanical degrees of freedom (C3D8T) and the coating is discretized with 3 960 elements of the same type.

Results of the simulation are illustrated in Figure 8 and Figure 9. Figure 8 left shows the distribution of temperature and Figure 8 right shows the distribution of von Mises stress during the second loading step. Additionally, Figure 9 left illustrates the distribution of the deviatoric part of the internal variable e_v^{dev} and Figure 9 right illustrates the

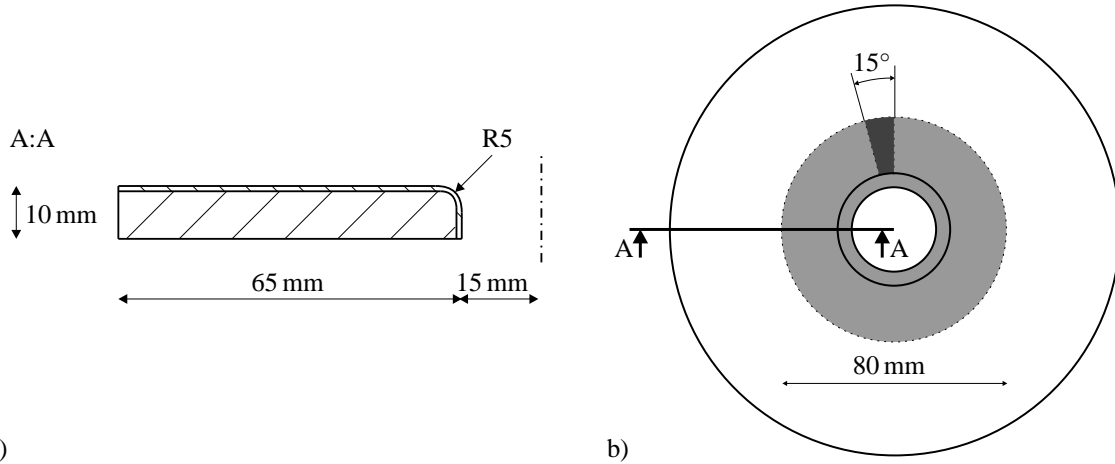


Figure 7: Coated hybrid forming tool, a) geometry, b) area for thermal and mechanical loading (on boundary conditions see text)

Table 2: Hybrid forming tool: mechanical material parameters

κ^{el} :	G [MPa]	K [MPa]	α^{th} [1/K]						
	80 769	175 000	20×10^{-6}						
κ^{el} :	G [MPa]	K [MPa]	α^{th} [1/K]						
	69 231	150 000	12×10^{-6}						
κ^{vpd} :	G [MPa]	K [MPa]	Y_0 [MPa]	H [MPa]	b [-]	q [MPa]	a_1 [-]	a_1^* [-]	a_2 [-]
	69 231	150 000	400	500	1	0	0.4	0.4	0.6
	a_2^* [-]	K_λ [MPa]	m [-]	e^{dev} [-]	w^{dev} [-]	d^{dev} [-]	n^{dev} [-]	e^{vol} [-]	w^{vol} [-]
	0.6	10^{-9}	2	0.0005	5×10^6	0.0001	3	0.0005	5×10^6
	d^{vol} [-]	n^{vol} [-]	α^{th} [1/K]						
	0.0001	3	12×10^{-6}						

distribution of the dependent damage variable D . Since the temperature is directly specified in terms of thermal boundary conditions applied onto the top surface of the coating resulting temperatures are between 20°C (initial condition) and 600°C (boundary condition). Maximum resulting von Mises stresses occur below the loaded area of the coating in the substrate, since this material is modelled purely elastic, thus leading to higher stresses in the substrate than in the coating. Of course results for the deviatoric part of the internal variable e_v^{dev} and for the dependent damage variable D are only obtained for the coating, since this material is modelled using the elasto-viscoplastic material model with damage. Maximum values for the damage variable are smaller than 60% since elements with values exceeding this barrier are deleted. To summarize, the inhomogeneous thermal and mechanical boundary conditions lead to an inhomogeneous mechanical stress and strain fields, thus leading to inhomogeneous element deletion indicating failure of the coating system. Failure begins in that region, which is loaded maximum and then it follows the path of the loaded circle until finally large parts of the coating have failed.

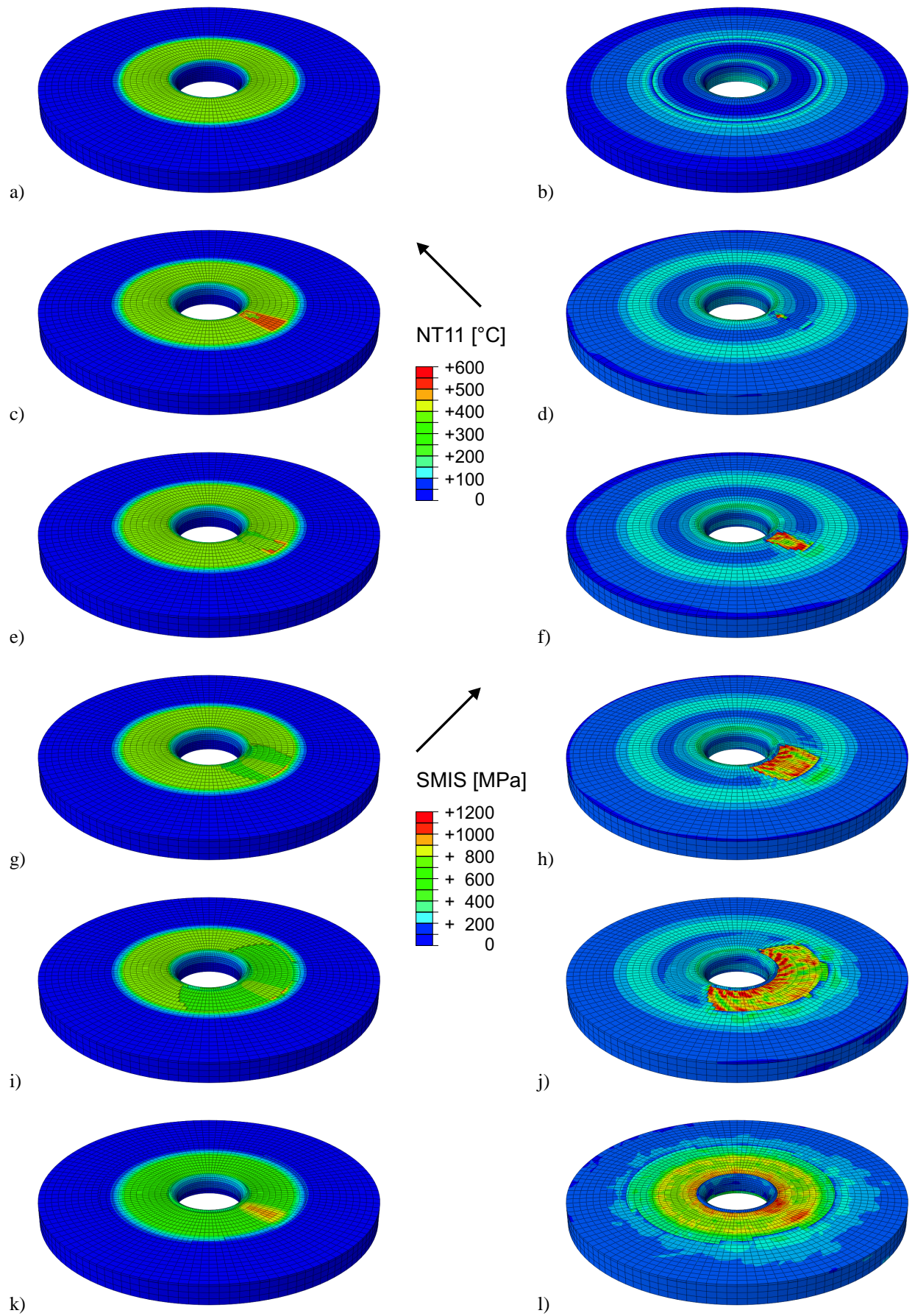


Figure 8: Hybrid forming tool, left: evolution of temperature, right: evolution of von Mises stress, a), b) at the beginning of step 2, c) to j) during step 2, k), l) at the end of step 2

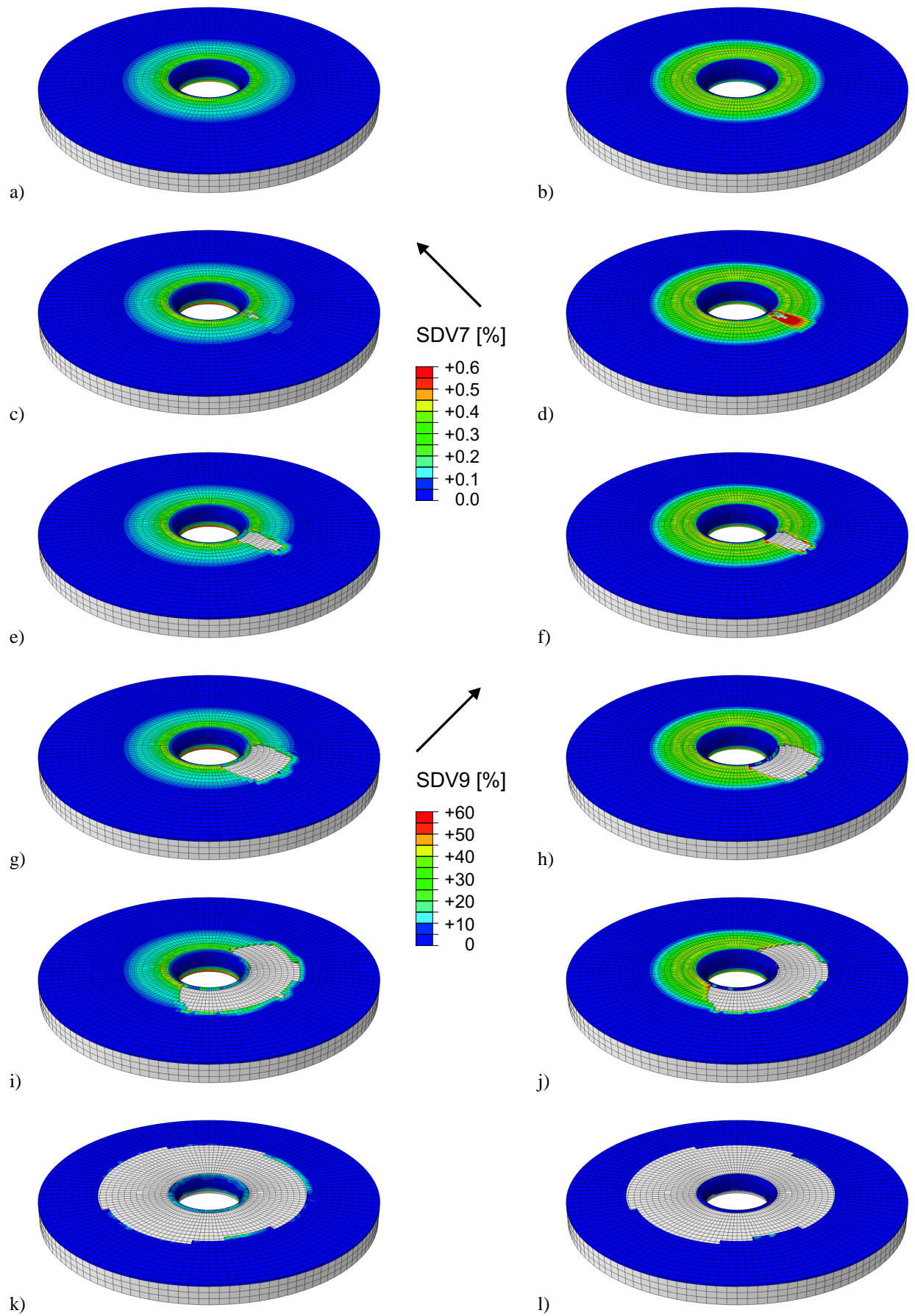


Figure 9: Hybrid forming tool, left: evolution of deviatoric part of internal variable e_v^{dev} , right: evolution of dependent damage variable D , a), b) at the beginning of step 2, c) to j) during step 2, k), l) at the end of step 2

5 Summary and Conclusions

A two scale finite element model for coated hybrid forming tools has been introduced, which considers several individual coating layers on the mesoscale. On the macroscale the coating system is discretized within one finite element over the complete coating thickness, thus leading to a reduction of computational costs. Scale transitions for the thermal and for the mechanical problem are outlined, e.g. using Taylor assumptions for the localization process and volume averaging procedures for the homogenization process. The applied mechanical material models on the mesoscale are briefly outlined and the incorporation of a mesoscopic damage variable into the macroscopic thermal material model for modelling a modified heat transfer through a partially damaged layer in an implicit setting is introduced. Remarks on numerical implementation are briefly outlined and two numerical examples are addressed using an implicit and an explicit solution strategy. Results show the capability of the proposed model to be applied for coated forming tools subjected to thermo-mechanical loading conditions.

Our future work is directed to parameter identification for the individual coating layers considering a particular coating system applied onto the substrate of the forming tool. Another goal is the finite element simulation of an industrial hybrid forming process using the introduced two scale framework for coated forming tools. Finally, experimental validation of the simulation will be carried out and lifetime estimation of the coated hybrid forming tool will be performed using numerical results as input quantities for thermo-mechanical fatigue (TMF) tests.

Acknowledgements

This paper is based on investigations of the collaborative research centre SFB/TR TRR 30, which is kindly supported by the Deutsche Forschungsgemeinschaft (DFG), Germany.

References

- Allen, D.: Homogenization principles and their application to continuum damage mechanics. *Composites Science and Technology*, 61, (2001), 2223 – 2230.
- Bobzin, K.; Lugscheider, E.; Nickel, R.; Kashko, T.: Advanced homogenization strategies in material modeling of thermally sprayed tbc. *Advanced Engineering Materials*, 8, (2006), 663 – 669.
- Chaboche, J.-L.: Thermodynamic formulation of constitutive equations and application to the viscoplasticity and viscoelasticity of metals and polymers. *Int. J. Solids Structures*, 34, (1997), 2239 – 2254.
- Feng, Z.; Domaszewski, M.; Montavon, G.; Coddet, C.: Finite element analysis of effect of substrate surface roughness on liquid droplet impact and flattening process. *Journal of Thermal Spray Technology*, 11, (2000), 62 – 68.
- Feyel, F.; Chaboche, J.-L.: Fe² multiscale approach for modelling the elastoviscoplastic behaviour of long fibre sic/ti composite materials. *Comput. Meth. Appl. Mech. Eng.*, 183, (2000), 309 – 330.
- Hartley, P.; Pillinger, I.: Numerical simulation of the forging process. *Comput. Methods Appl. Mech. Engrg.*, 195, (2006), 6676 – 6690.
- Hill, R.: Elastic properties of reinforced solids: Some theoretical principles. *J. Mech. Phys. Solids*, 11, (1963), 357 – 372.
- Kouznetsova, V.; Brekelmans, W.; Baaijens, F.: An approach to micro-macro modelling of heterogeneous materials. *Comput. Mech.*, 27, (2001), 37 – 48.
- Lee, S.; Sundararaghavan, V.: Multi-scale homogenization of moving interface problems with flux jumps: Application to solidification. *Comput. Mech.*, 44, (2009), 297 – 307.
- Li, G.; Jinn, J.; Wu, W.; Oh, S.: Recent development and applications of three-dimensional finite element modeling in bulk forming process. *J. Mater. Process Tech.*, 113, (2001), 40 – 45.
- Liu, H.; Yan, H.; Wang, X.; Lu, S.; Yang, K.; Cai, L.: Finite element analysis of the effects of coated tool on high speed orthogonal machining. *Key Engineering Materials*, 392-394, (2009), 879 – 883.
- Lu, P.; Zhao, G.; Guan, Y.; Wu, X.: Bulk metal forming process simulation based on rigid-plastic/viscoplastic element free galerkin method. *Mater. Sci. Eng. A*, 479, (2008), 197 – 212.

- Lugscheider, E.; Bobzin, K.; Nickel, R.: Application of multiscale modeling in the coating formation simulation of aps pysz tbc. *Journal of Thermal Spray Technology*, 15, (2006), 537 – 544.
- Mackerle, J.: Coatings and surface modification technologies: a finite element bibliography (1995-2005). *Modelling Simul. Mater. Sci. Eng.*, 13, (2005), 935 – 979.
- Mahnken, R.: Improved implementation of an algorithm for non-linear isotropic/kinematic hardening in elasto-plasticity. *Commun. Numer. Meth. Engng.*, 15, (1999), 745 – 754.
- Mahnken, R.: Simulation of strength difference coupled to softening in elasto-plasticity for adhesive materials. *International Journal of Adhesion and Adhesives*, submitted.
- Mahnken, R.; Schlimmer, M.: Simulation of strength difference in elasto-plasticity for adhesive materials. *Int. J. Numer. Meth. Engng.*, 63, (2005), 1461 – 1477.
- Maugin, G.: *The Thermodynamics of Plasticity and Fracture*. Cambridge University Press, Cambridge (1992).
- Miehe, C.; Dettmar, J.: A framework for micro-macro transitions in periodic particle aggregates of granular materials. *Comput. Meth. Appl. Mech. Eng.*, 193, (2004), 225 – 256.
- Miehe, C.; Koch, A.: Computational micro-to-macro transitions of discretized microstructures undergoing small strains. *Archive of Applied Mechanics*, 72, (2002), 300 – 317.
- Ostoja-Starzewski, M.: Towards stochastic continuum thermodynamics. *J. Non-Equilib. Thermodyn.*, 27, (2002), 335 – 348.
- Özdemir, I.; Brekelmans, W.; Geers, M.: Computational homogenization for heat conduction in heterogeneous solids. *Int. J. Numer. Meth. Engng.*, 73, (2008a), 185 – 204.
- Özdemir, I.; Brekelmans, W.; Geers, M.: Fe² computational homogenization for the thermo-mechanical analysis of heterogeneous solids. *Comput. Meth. Appl. Mech. Eng.*, 198, (2008b), 602 – 613.
- Özdemir, I.; Brekelmans, W.; Geers, M.: A thermo-mechanical cohesive zone model. *Comput. Mech.*, 46, (2010), 735 – 745.
- Saanouni, K.: On the numerical prediction of the ductile fracture in metal forming. *Eng. Frac. Mech.*, 75, (2008), 3545 – 3559.
- Schröder, J.: Derivation of the localization and homogenization conditions for electro-mechanically coupled problems. *Coput. Mater. Sci.*, 46, (2009), 595 – 599.
- Steinhoff, K.; Weidig, U.; Scholtes, B.; Zinn, W.: Innovative flexible metal forming processes based on hybrid thermo-mechanical interaction. *Steel Research*, 76, (2005), 154 – 159.
- Suquet, P.: Elements of homogenization for inelastic solid mechanics. In: E. Sanchez-Palencia; A. Zaoui, eds., *Homogenization Techniques for Composite Media*, Springer, Berlin, Heidelberg, New York (1985).
- Truesdell, C.; Noll, W.: The non-linear field theories of mechanics. In: S. Flügge, ed., *Encyclopedia of Physics*, Springer, Berlin, Heidelberg, New York (1965).
- Ucun, I.; Aslantas, K.: Numerical simulation of orthogonal machining process using multilayer and single-layer coated tools. *Int. J. Adv. Manuf. Technol.*, 54, (2011), 899 – 910.
- Weidig, U.; Hübner, L.; Steinhoff, K.: Bulk steel products with functionally graded properties produced by differential thermo-mechanical processing. *Steel Research*, 79, (2008), 59 – 65.
- Wenzelburger, M.; Escribano, M.; Gadow, R.: Modeling of thermally sprayed coatings on light metal substrates: Layer growth and residual stress formation. *Surf. Coating Tech.*, 180-181, (2004), 429 – 435.
- Xie, W.; Jordan, E.; Gell, M.: Stress and cracking behavior of plasma sprayed thermal barrier coatings using an advanced constitutive model. *Comput. Struct.*, 83, (2006), 574 – 587.
- Xiong, S.; Liu, W.; Cao, J.; Li, C.; Rodrigues, J.; Martins, P.: Simulation of bulk metal forming processes using the reproducing kernel particle method. *Mater. Sci. Eng. A*, 419, (2005), 50 – 58.

Address: Dipl.-Ing. Kim-Henning Sauerland and Prof. Dr.-Ing. Rolf Mahnken, M.Sc., Lehrstuhl für Technische Mechanik, Universität Paderborn, D-33098 Paderborn.
email: sauerland@ltm.upb.de; mahnken@ltm.upb.de.